

Partial Functional Correspondence

E. Rodolà¹, L. Cosmo², M. M. Bronstein³, A. Torsello², D. Cremers¹

¹TU Munich, ²University of Venice, ³USI Lugano

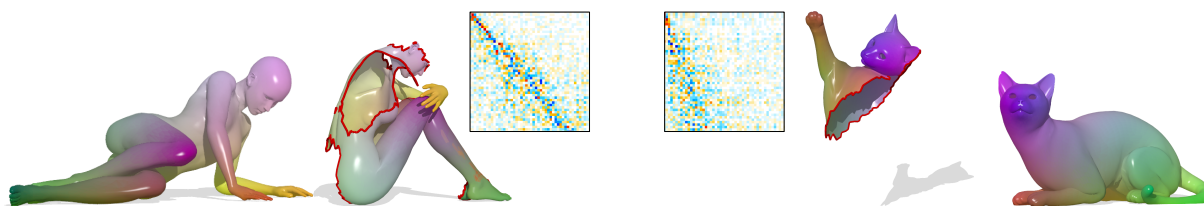


Figure 1: Partial functional correspondence between two pairs of shapes with large missing parts. For each pair we show the matrix C representing the functional map in the spectral domain, and the action of the map by transferring colors from one shape to the other. The special slanted-diagonal structure of C induced by the partiality transformation is first estimated from spectral properties of the two shapes, and then exploited to drive the matching process.

Abstract

In this paper, we propose a method for computing partial functional correspondence between non-rigid shapes. We use perturbation analysis to show how removal of shape parts changes the Laplace-Beltrami eigenfunctions, and exploit it as a prior on the spectral representation of the correspondence. Corresponding parts are optimization variables in our problem and are used to weight the functional correspondence; we are looking for the largest and most regular (in the Mumford-Shah sense) parts that minimize correspondence distortion. We show that our approach can cope with very challenging correspondence settings.

Categories and Subject Descriptors (according to ACM CCS): I.3.5 [Computer Graphics]: Computational Geometry and Object Modeling—Shape Analysis

1. Introduction

The problem of shape correspondence is one of the most fundamental problems in computer graphics and geometry processing, with a plethora of applications ranging from texture mapping to animation. A particularly challenging setting is that of non-rigid correspondence, where the shapes in question are allowed to undergo deformations, which are typically assumed to be approximately isometric (such a model appears to be good for, *e.g.*, human body poses). Even more challenging is *partial correspondence*, where one is shown only a subset of the shape and has to match it to a deformed full version thereof. Partial correspondence problems arise in numerous applications that involve real data acquisition by 3D sensors, which inevitable lead to missing parts due to occlusions or partial view.

Related work. Shape correspondence is one of the most researched topics in geometry processing, with many popular methods such as [BBK06, KLCF10, KLF11]. Here, we limit our attention to the partial correspondence setting; for a comprehensive overview of correspondence problems, we refer the reader to the recent survey [VKZHC01].

In the domain of partial rigid shape alignment and matching, *e.g.*, for 3D scan completion applications, many versions of regularized ICP approaches exist, see for example [AMCO08, ART15]. Deformation-driven shape matching [ZSCO*08] can be used in the non-rigid case. Our present work draws inspiration from [BB08, BBBK09], which combines metric distortion minimization with part optimization.

More recent works have explored alignment of tangent spaces [BWW*14], weighted matching of bags of local de-

scriptors [PBB13], sparse minimum distortion correspondence [RBA*12], bilateral maps [vKZH13], shape extremities [SY14], and other constructions for the purpose of non-rigid partial matching. In the context of collections of shapes, partial correspondence has been considered in [VKTS*11, HG13].

Our work is based on the functional maps framework [OBCS*12], in which shape correspondence is modeled as a linear operator between spaces of functions on the shapes. Such operators can be efficiently represented in the Laplace-Beltrami eigenbasis [OBCS*12]. Huang and Guibas [HWG14] used functional maps to analyze large collections of shapes in which some shapes may be only partially similar, constructing graphs of functional maps.

Contribution. In this paper, we propose an extension to the functional correspondence framework to allow dealing with partial correspondence. Specifically, we consider a scenario of matching a part of a deformed shape to some full model. Such scenarios are very common for instance in robotics applications, where one has to match an object acquired by means of a 3D scanner (and thus partially occluded) with a reference object known in advance. We use an explicit part model over which optimization is performed, as well as a regularization on the spectral representation of the functional correspondence accounting for a special structure of the Laplacian eigenfunctions as a result of part removal. Theoretical study of this behavior based on perturbation analysis of Laplacian matrices is another contribution of our work. We show experimentally that the proposed approach allows dealing with very challenging partial correspondence settings.

The rest of the paper is organized as follows. In Section 2, we review the basic concepts in the spectral geometry of shapes and describe the functional correspondence approach. Section 3 introduces our partial correspondence model, and Section 4 describes its implementation details. Section 5 studies the behavior of Laplacian eigenfunctions in the case of missing parts, motivating the regularizations used in the previous sections. Section 6 presents experimental results, and finally, Section 7 concludes the paper.

2. Background

In this paper, we model a shape as a two-dimensional Riemannian manifold \mathcal{M} (possibly with boundary). At interior points, the manifold is locally homeomorphic to a two-dimensional Euclidean space known as the *tangent plane* $T_x\mathcal{M}$. The Riemannian metric is given in the form of an inner product $\langle \cdot, \cdot \rangle_{T_x\mathcal{M}} : T_x\mathcal{M} \times T_x\mathcal{M} \rightarrow \mathbb{R}$ on the tangent plane, varying smoothly with x . The *exponential map* is a mapping $\exp_x : T_x\mathcal{M} \rightarrow \mathcal{M}$ from the tangent plane to the manifold.

Given a smooth real function $f : \mathcal{M} \rightarrow \mathbb{R}$, let us define the

function on the tangent plane by the composition $f \circ \exp_x : T_x\mathcal{M} \rightarrow \mathbb{R}$. Then, the *intrinsic gradient* is defined as

$$\nabla_{\mathcal{M}}f = \nabla(f \circ \exp_x)(0), \quad (1)$$

where ∇ denotes the standard Euclidean gradient in the tangent plane. The intrinsic gradient is thus a vector in the tangent plane. Similarly, the positive semi-definite *Laplace-Beltrami operator* $\Delta_{\mathcal{M}} : L^2(\mathcal{M}) \rightarrow L^2(\mathcal{M})$ is defined as

$$\Delta_{\mathcal{M}}f = -\Delta(f \circ \exp_x)(0), \quad (2)$$

where Δ is the standard Laplacian. The Laplace-Beltrami operator is related to the intrinsic gradient through the *Stokes formula*,

$$\int_{\mathcal{M}} \Delta_{\mathcal{M}}f(x)g(x)dx = - \int_{\mathcal{M}} \langle \nabla_{\mathcal{M}}f(x), \nabla_{\mathcal{M}}g(x) \rangle_{T_x\mathcal{M}}dx,$$

for any smooth $f, g \in L^2(\mathcal{M})$.

The Laplace-Beltrami operator admits an eigen-decomposition $\Delta_{\mathcal{M}}\phi_i(x) = -\lambda_i\phi_i(x)$ for $i \geq 1$, with eigenvalues $0 = \lambda_1 < \lambda_2 \leq \dots$ and eigenfunctions $\{\phi_i\}_{i \geq 1}$ forming an orthonormal basis on $L^2(\mathcal{M})$, i.e., $\langle \phi_i, \phi_j \rangle_{L^2(\mathcal{M})} = \delta_{ij}$.

Fourier analysis. Let $L^2(\mathcal{M}) = \{f : \mathcal{M} \rightarrow \mathbb{R} : \int_{\mathcal{M}} f(x)^2 dx < \infty\}$ denote the space of functions on \mathcal{M} , and let $\langle f, g \rangle_{L^2(\mathcal{M})} = \int_{\mathcal{M}} f(x)g(x)dx$ be the standard inner product. Given an orthonormal basis $\{\phi_i\}_{i \geq 1} \subseteq L^2(\mathcal{M})$, a function $f \in L^2(\mathcal{M})$ can be expanded into the *Fourier series* as

$$f(x) = \sum_{i \geq 1} \langle f, \phi_i \rangle_{L^2(\mathcal{M})} \phi_i(x). \quad (3)$$

Functional correspondence. Let us be now given two manifolds, \mathcal{N} and \mathcal{M} . Ovsjanikov *et al.* [OBCS*12] proposed modeling *functional correspondence* between shapes as a linear operator $T : L^2(\mathcal{N}) \rightarrow L^2(\mathcal{M})$ between spaces of functions on \mathcal{N} and \mathcal{M} . One can easily see that classical vertex-wise correspondence is a particular setting where T maps delta-functions to delta-functions.

Assuming to be given two orthonormal bases $\{\phi_i\}_{i \geq 1}$ and $\{\psi_j\}_{j \geq 1}$ on $L^2(\mathcal{N})$ and $L^2(\mathcal{M})$ respectively, the functional correspondence can be expressed w.r.t. to these bases as follows:

$$\begin{aligned} Tf &= T \sum_{i \geq 1} \langle f, \phi_i \rangle_{L^2(\mathcal{N})} \phi_i = \sum_{i \geq 1} \langle f, \phi_i \rangle_{L^2(\mathcal{N})} T\phi_i \\ &= \sum_{ij \geq 1} \langle f, \phi_i \rangle_{L^2(\mathcal{N})} \underbrace{\langle T\phi_i, \psi_j \rangle_{L^2(\mathcal{M})}}_{c_{ij}} \psi_j, \end{aligned} \quad (4)$$

where $f \in L^2(\mathcal{N})$ is some function on \mathcal{N} . Thus, T amounts to a linear transformation of the Fourier coefficients of f from basis $\{\phi_i\}_{i \geq 1}$ to basis $\{\psi_j\}_{j \geq 1}$, which is captured by the coefficients c_{ij} . Truncating the Fourier series at the first k coefficients, one obtains a rank- k approximation of T as a $k \times k$ matrix $\mathbf{C} = (c_{ij})$.

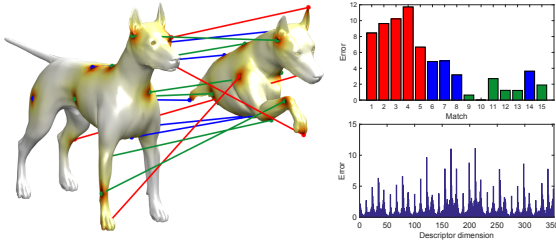


Figure 2: Action of the mixed norm $\|\mathbf{CA} - \mathbf{B}(\eta(v))\|_{2,1}$. Left: Noisy landmark matches between complete and partial shape, represented as Gaussian functions centered at corresponding points. Correct matches are shown in green, mismatches in red, and correct matches along the boundary in blue. Top right: Bar plot showing $\|\mathbf{CA}_i - \mathbf{B}(\eta(v))_i\|_2$, where i ranges over the matches and \mathbf{C} is an optimal map found by our method. Even under an outlier ratio of $\sim 30\%$, all mismatches are correctly detected and accounted for. Bottom right: Same plot when using dense descriptors.

In order to compute \mathbf{C} , Ovsjanikov *et al.* [OBBS*12] assume to be given a set of q corresponding functions $\{f_1, \dots, f_q\} \subseteq L^2(\mathcal{N})$ and $\{g_1, \dots, g_q\} \subseteq L^2(\mathcal{M})$. Denoting by $a_{ij} = \langle f_j, \phi_i \rangle_{L^2(\mathcal{N})}$ and $b_{ij} = \langle g_j, \psi_i \rangle_{L^2(\mathcal{M})}$ the $k \times q$ matrices of the respective Fourier coefficients, functional correspondence boils down to the linear system

$$\mathbf{CA} = \mathbf{B}. \quad (5)$$

If $q \geq k$, this system (5) is determined and is solved in the least squares sense to determine \mathbf{C} .

Structure of \mathbf{C} . We note that the coefficients \mathbf{C} depend on the choice of the bases. In particular, it is convenient to use the Laplace-Beltrami eigenbasis as a natural Fourier basis; truncating the series at the first k coefficients has the effect of ‘low-pass’ filtering thus producing smooth correspondences. In the following, we will tacitly assume that $\{\phi_i\}_{i \geq 1}$ and $\{\psi_i\}_{i \geq 1}$ are the eigenfunctions of the respective Laplacians.

Furthermore, note that the system (5) has qk equations and k^2 variables. However, in many situations the actual number of variables is significantly smaller, as \mathbf{C} manifests a certain structure which can be taken advantage of. In particular, if \mathcal{N} and \mathcal{M} are isometric and have simple spectrum (*i.e.*, the Laplace-Beltrami eigenvalues have no multiplicity), then $T\phi_i = \pm\psi_i$, or in other words, $c_{ij} = \pm\delta_{ij}$. In more realistic scenarios (approximately isometric shapes), the matrix \mathbf{C} would manifest a funnel-shaped structure, with the majority of elements distant from the diagonal close to zero.

3. Partial functional maps

For simplicity, throughout the paper we consider the setting where we are given a full model shape \mathcal{M} and another query shape \mathcal{N} that corresponds to an approximately isometrically

deformed part $\mathcal{M}' \subset \mathcal{M}$. A more general setting where \mathcal{M} and \mathcal{N} have some common parts \mathcal{M}' and \mathcal{N}' is a rather straightforward extension of the presented approach.

Following [BB08], we model the part \mathcal{M}' by means of an indicator function $v: \mathcal{M} \rightarrow \{0, 1\}$ such that $v(x) = 1$ if $x \in \mathcal{M}'$ and zero otherwise. Assuming that v is known, the *partial functional correspondence* between \mathcal{N} and \mathcal{M} can be expressed as $Tf = vg$, where v can be regarded as a kind of mask, and anything outside the region where $v = 1$ should be ignored. Expressed w.r.t. bases $\{\phi_i\}_{i \geq 1}$ and $\{\psi_i\}_{i \geq 1}$, the partial functional correspondence takes the form $\mathbf{CA} = \mathbf{B}(v)$, where $\mathbf{B}(v)$ denotes a matrix of weighted inner products with elements given by $b_{ij}(v) = \int_{\mathcal{M}} v(x) \psi_i(x) g_j(x) dx$ (when $v(x) \equiv 1$, \mathbf{B} is simply the matrix of Fourier coefficients defined in (5)).

This brings us to the problem we are considering throughout this paper, involving optimization w.r.t. correspondence (encoded by the coefficients \mathbf{C}) and the part v ,

$$\min_{\mathbf{C}, v} \|\mathbf{CA} - \mathbf{B}(\eta(v))\|_{2,1} + \rho_{\text{corr}}(\mathbf{C}) + \rho_{\text{part}}(v), \quad (6)$$

where $\eta(t) = \frac{1}{2}(\tanh(2t) + 1)$ saturates the part indicator function between zero and one. Here ρ_{corr} and ρ_{part} denote regularization terms for the correspondence and the part, respectively; these terms are explained below. We use the $L_{2,1}$ matrix norm (equal to the sum of L_2 -norms of matrix columns) to handle possible outliers in the corresponding data, as such a norm promotes column-sparse matrices (see Fig. 2 for an example).

Note that in order to avoid a combinatorial optimization over binary-valued v , we use a continuous v with values in the range $(-\infty, +\infty)$, saturated by the non-linearity η . This way, $\eta(v)$ becomes a soft membership function with values in the range $[0, 1]$.

Part regularization. Similarly to [BB08], we try to find the part with area closest to that of the query and with shortest boundary. This can be expressed as

$$\rho_{\text{part}}(v) = \mu_1 \left(\text{area}(\mathcal{N}) - \int_{\mathcal{M}} \eta(v) dx \right)^2 + \mu_2 \int_{\mathcal{M}} \xi(v) \|\nabla_{\mathcal{M}} v\| dx, \quad (7)$$

where $\xi(t) \approx \delta\left(\eta(t) - \frac{1}{2}\right)$ and the norm is on the tangent space. The μ_2 -term in (7) is an intrinsic version of the *Mumford-Shah functional* [MS89], measuring the length of the boundary of a part represented by a (soft) membership function. This functional was used previously in image segmentation applications [VC02].

Correspondence regularization. For the correspondence, we use the penalty

$$\begin{aligned} \rho_{\text{corr}}(\mathbf{C}) = & \mu_3 \|\mathbf{C} \circ \mathbf{W}\|_{\text{F}}^2 + \mu_4 \sum_{i \neq j} (\mathbf{C}^{\top} \mathbf{C})_{ij}^2 \\ & + \mu_5 \sum_i ((\mathbf{C}^{\top} \mathbf{C})_{ii} - d_i)^2, \end{aligned} \quad (8)$$

where \circ denotes Hadamard (element-wise) matrix product. The μ_3 -term models a special slanted-diagonal structure of \mathbf{C} that we observe in partial matching problems (see Fig. 4); the theoretical motivation for this behavior is presented in Section 5. Here, \mathbf{W} is a weight matrix with zeros along the slanted diagonal and large values outside (see Figure 3; details on the computation of \mathbf{W} are provided in Appendix A). The μ_4 -term promotes orthogonality of \mathbf{C} by penalizing the off-diagonal elements of $\mathbf{C}^{\top} \mathbf{C}$. The reason is that for isometric shapes, the functional map is volume-preserving, and this is manifested in orthogonal \mathbf{C} [OBCS*12]. Note that differently from the baseline case dealing with full shapes, in our setting we can only require orthogonality (hence area preservation) going in the direction from partial to complete model; for this reason, we do not impose any restrictions on $\mathbf{C}\mathbf{C}^{\top}$ and we say that the matrix is *semi*-orthogonal. Finally, the μ_5 -term models the rank of the matrix \mathbf{C} , where vector $\mathbf{d} = (d_1, \dots, d_k)$ determines how many singular values of \mathbf{C} are non-zero (the estimation of \mathbf{d} is described in Appendix A).

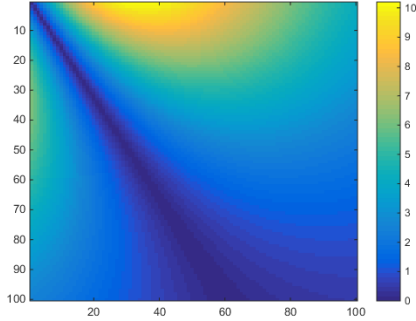


Figure 3: Weight matrix \mathbf{W} obtained with $k = 100$, $r = 60$, and $\sigma = 0.03$ (see Appendix A for details)

Remark. The fact that matrix \mathbf{C} is of low rank is a direct consequence of partiality. This can be understood by recalling that the (non-truncated) functional map representation amounts to an orthogonal change of basis; since in the standard basis the correspondence matrix is low-rank (as it contains zero-sum rows), this property is preserved by the change of basis.

In Fig. 4 we show an example of a valid partial functional map \mathbf{C} , illustrating its main properties.

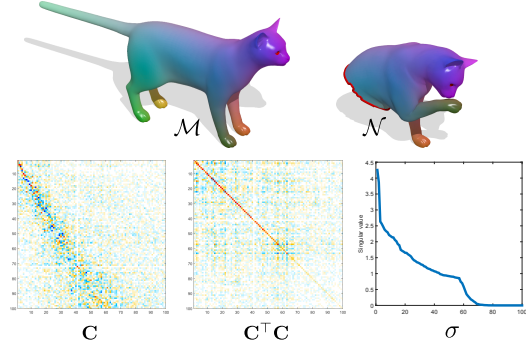


Figure 4: Left: A partial functional map \mathbf{C} from \mathcal{N} to \mathcal{M} is low-rank and manifests a slanted-diagonal structure due to eigenvector interactions along the boundary of \mathcal{N} . Middle: If the map is volume-preserving then its full-rank sub-matrix is semi-orthogonal. Observe the trail of small values along the diagonal. Right: Singular values of \mathbf{C} .

Alternating scheme. To solve the optimization problem (6), we perform an alternating optimization w.r.t. to \mathbf{C} and v , repeating the following steps until convergence:

C-step: Fix v^* , solve for correspondence \mathbf{C}

$$\min_{\mathbf{C}} \|\mathbf{C}\mathbf{A} - \mathbf{B}(\eta(v^*))\|_{2,1} + \rho_{\text{corr}}(\mathbf{C}). \quad (9)$$

V-step: Fix \mathbf{C}^* , solve for part v

$$\min_v \|\mathbf{C}^*\mathbf{A} - \mathbf{B}(\eta(v))\|_{2,1} + \rho_{\text{part}}(v). \quad (10)$$

An example of this alternating process applied to a pair of shapes is shown in Fig. 5.

4. Implementation

Discretization. In the discrete setting, the manifold \mathcal{M} is sampled at n points x_1, \dots, x_n . On these points, we construct a manifold triangular mesh (V, E, F) with vertices $V = \{1, \dots, n\}$, in which each interior edge $ij \in E$ is shared by exactly two triangular faces ikj and $jhi \in F$, and boundary edges belong to exactly one triangular face. We denote by \mathbf{X} the $n \times 3$ matrix of the embedding coordinates of the mesh.

A function on the manifold is represented by an n -dimensional vector $\mathbf{f} = (f(x_1), \dots, f(x_n))^{\top}$. The discretization of the Laplacian takes the form $\mathbf{L} = \mathbf{S}^{-1}\mathbf{H}$ using the classical cotangent formula [Mac49, Duf59, PP93, MDSB03],

$$h_{ij} = \begin{cases} (\cot \alpha_{ij} + \cot \beta_{ij})/2 & ij \in E; \\ -\sum_{k \neq i} h_{ik} & i = j; \\ 0 & \text{else;} \end{cases} \quad (11)$$

where $\mathbf{S} = \text{diag}(s_1, \dots, s_n)$ and $s_i = \frac{1}{3} \sum_{jk:ijk \in F} s_{ijk}$ denotes the local area element at vertex i and s_{ijk} denoting the area

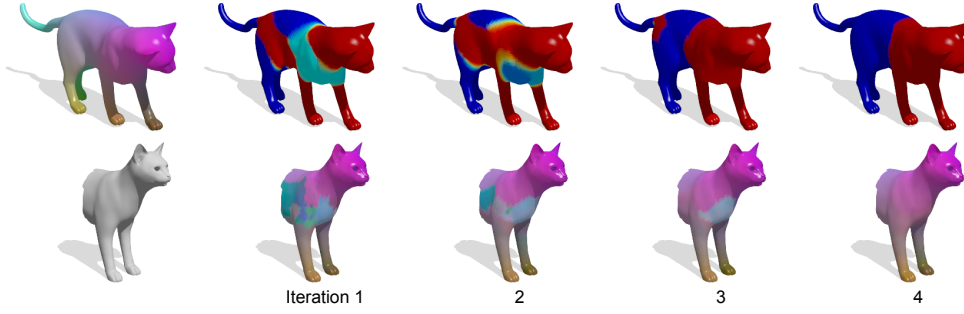


Figure 5: An example of the matching process operating on two shapes from TOSCA. The algorithm alternately optimizes over corresponding part (top row) and functional correspondence (bottom row). Corresponding points between full and partial shape are shown with the same color. This solution was obtained by using 30 eigenfunctions on both manifolds.

of triangle ijk , and α_{ij}, β_{ij} denote the angles $\angle ikj, \angle jhi$ of the triangles sharing the edge ij .

The first k eigenfunctions and eigenvalues of the Laplacian are computed by performing the generalized eigen-decomposition $\mathbf{H}\Phi = \mathbf{S}\Phi\Lambda$, where $\Phi = (\phi_1, \dots, \phi_k)$ is an $n \times k$ matrix containing as columns the discretized eigenfunctions and $\Lambda = \text{diag}(\lambda_1, \dots, \lambda_k)$ is the diagonal matrix of the corresponding eigenvalues.

Discretization of regularization terms. Our goal is to discretize the μ_1 - and μ_2 -terms in (7). The part membership function is discretized as an n -dimensional vector \mathbf{v} . The μ_1 term is simply discretized as $\int_{\mathcal{M}} \eta(\mathbf{v}) dx \approx \mathbf{s}^\top \eta(\mathbf{v})$, where the non-linearity η is applied element-wise.

We first express the discrete intrinsic gradient per face of the mesh. Let $ijk \in F$ be a triangle, and denote by $\mathbf{P} = (\mathbf{x}_k - \mathbf{x}_i, \mathbf{x}_j - \mathbf{x}_i)$ the 3×2 matrix of triangle edge vectors. Let $\mathbf{u} = (v_k - v_i, v_j - v_i)^\top$ be the 2-dimensional vector of the membership function gradient along the edges of the triangle. Then, the norm of the intrinsic gradient $\|\nabla_{\mathcal{M}} v\|$ for the triangle ijk is discretized as $g_{ijk}(\mathbf{v}) = (\mathbf{u}^\top (\mathbf{P}^\top \mathbf{P})^{-1} \mathbf{u})^{1/2}$; we denote by $\mathbf{g}(\mathbf{v})$ the $|F|$ -dimensional vector containing the norms of the gradient in all the triangles. In order to obtain the vertex-wise values of the intrinsic gradient norm, we construct an $n \times |F|$ matrix \mathbf{Q} whose element $q_{ij} = \frac{1}{3}$ if the j th triangle includes vertex i and zero otherwise. Then, $\int_{\mathcal{M}} \xi(\mathbf{v}) \|\nabla_{\mathcal{M}} v\| dx \approx \xi(\mathbf{v})^\top \mathbf{S}\mathbf{Q}\mathbf{g}(\mathbf{v})$ [BB08].

Numerical optimization. We implemented our matching framework in Matlab/C++ using the manifold optimization toolbox [BMAS14]. Each optimization step was performed by the method of conjugate gradients. In all our experiments we observed convergence in 3-5 iterations (around 5 mins. for a pair of shapes).

We start the alternating scheme by optimizing over \mathbf{C} and fixing $\mathbf{v}^* = \mathbf{1}$, where $\mathbf{1}$ is a vector of n ones. The initial value for \mathbf{C} at the first iteration of the alternating process is set

to the weight matrix $\mathbf{C} = \mathbf{W}$. In order to construct \mathbf{W} we need to have an estimate of the expected rank of the sought functional map, which in turn determines its diagonal slope. The same value is then used to construct \mathbf{d} . A simple method for computing such an estimate is given in the next section; see also Fig. 6 for an illustration of this approach.

Finally, in order to account for noisy data we run a refinement step after each C -step. Specifically, assume \mathbf{C}^* is a local optimum of problem (9). Then, we solve again for \mathbf{C} by setting $\mu_3 = 0$ and replacing the data term in (9) with $\|\mathbf{C}\Phi^\top - \Psi^\top \Pi\|_{2,1}$, where Π is a permutation matrix aligning columns of Ψ^\top with columns of $\mathbf{C}^*\Phi^\top$. Together with the semi-orthogonality requirement on \mathbf{C} , this refinement step can be seen as a generalization to partial maps of the ICP-like technique found in [OBCS*12].

5. Perturbation analysis of the Laplacian spectrum

By a slight abuse of notation, in this section we denote by \mathcal{M} the set of vertices on the full shape, and let $\mathcal{N} \subseteq \mathcal{M}$ be the set of vertices on the partial shape. With $\bar{\mathcal{N}}$ we denote the restriction to the remaining vertices $\mathcal{M} \setminus \mathcal{N}$. Our aim is to characterize the eigenvalues and eigenvectors of $\mathbf{L}_{\mathcal{M}}$, Laplacian of \mathcal{M} , in terms of perturbations of the eigenvalues and eigenvectors of the Laplacians $\mathbf{L}_{\mathcal{N}}$ and $\mathbf{L}_{\bar{\mathcal{N}}}$ of \mathcal{N} and $\bar{\mathcal{N}}$ respectively [MH88].

In this analysis we assume that the discrete Laplacian in use has a support of limited range. This means that the non-zero entries for the i -th row will correspond to vertices topologically close to the i -th vertex in the mesh, and that the discretization is of limited topological diameter (the maximum topological distance between non-zero entries). Note that this assumption holds for classical FEM schemes such as the cotangent rule [MDSB03], since in this case the i -th row will have non-zero entries in correspondence with i 's immediate neighbors, resulting in a range of the support of topological diameter 2. In case of the Graph Laplacian, the range has topological diameter equal to 1. As a result

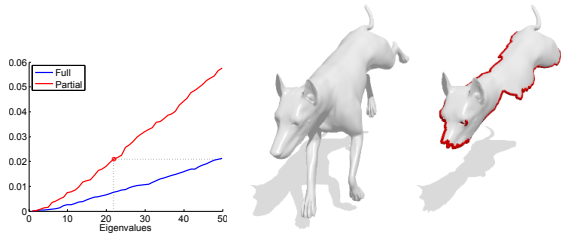


Figure 6: Neumann spectra of a full and partial shape, the latter being a connected subset of the former. The two spectra align only partially, a fact that allows to easily derive an estimate for the rank of the functional map relating the two shapes. In this example with 50 eigenfunctions, the estimated rank is 23 (the estimation procedure is shown as dashed lines).

of this property, there is a boundary band $\mathcal{B} = \partial\mathcal{N} \cup \partial\overline{\mathcal{N}}$ with $\partial\mathcal{N} \subseteq \mathcal{N}$ and $\partial\overline{\mathcal{N}} \subseteq \overline{\mathcal{N}}$, such that only the entries of the Laplacians $\mathbf{L}_{\mathcal{N}}$ and $\mathbf{L}_{\overline{\mathcal{N}}}$ between nodes in \mathcal{B} are affected by the cut. In particular, for the Graph Laplacian, the two boundary layers will be 1 vertex-thick, while for the cotangent Laplacian they will be 2 vertices-thick.

Without loss of generality we can assume that the vertices in \mathcal{M} are ordered such that the vertices in \mathcal{N} come before those in $\overline{\mathcal{N}}$. Further, within \mathcal{N} the boundary vertices $\partial\mathcal{N}$ are at the end, while within $\overline{\mathcal{N}}$ the boundary vertices $\partial\overline{\mathcal{N}}$ are at the beginning. With this ordering we can define the parametric matrix

$$\mathbf{L}(t) = \begin{pmatrix} \mathbf{L}_{\mathcal{N}} & \mathbf{0} \\ \mathbf{0} & \mathbf{L}_{\overline{\mathcal{N}}} \end{pmatrix} + t \begin{pmatrix} \mathbf{0} & \mathbf{0} & \mathbf{0} & \mathbf{0} \\ \mathbf{0} & \mathbf{D}_{\mathcal{N}} & \mathbf{E} & \mathbf{0} \\ \mathbf{0} & \mathbf{E}^{\top} & \mathbf{D}_{\overline{\mathcal{N}}} & \mathbf{0} \\ \mathbf{0} & \mathbf{0} & \mathbf{0} & \mathbf{0} \end{pmatrix}, \quad (12)$$

where the second and third rows/columns of the last matrices are over the vertices in $\partial\mathcal{N}$ and $\partial\overline{\mathcal{N}}$ respectively. Here $\mathbf{D}_{\mathcal{N}}$ and $\mathbf{D}_{\overline{\mathcal{N}}}$ represent the variations, with respect to the full Laplacian $\mathbf{L}_{\mathcal{M}}$, of the Laplacians $\mathbf{L}_{\mathcal{N}}$ and $\mathbf{L}_{\overline{\mathcal{N}}}$ within nodes in $\partial\mathcal{N}$ and $\partial\overline{\mathcal{N}}$ respectively, while \mathbf{E} represents the variations across the boundary.

These matrices are such that $\mathbf{L}(1) = \mathbf{L}_{\mathcal{M}}$, while for $t = 0$ the eigenvalues and eigenvectors of $\mathbf{L}(0)$ correspond to the eigenvalues and (extended) eigenvectors of $\mathbf{L}_{\mathcal{N}}$ and $\mathbf{L}_{\overline{\mathcal{N}}}$. Given a correct order of the nodes, due to the limit in the range of the support of the Laplacian, the matrices $\mathbf{D}_{\mathcal{N}}$ and $\mathbf{D}_{\overline{\mathcal{N}}}$ will have a band-diagonal structure, with the exception of a few wrap-around points due to cyclic ordering along the cut. In particular, in the case of the Graph Laplacian, $\mathbf{D}_{\mathcal{N}}$ and $\mathbf{D}_{\overline{\mathcal{N}}}$ will be diagonal with almost constant diagonal elements if the mesh is sufficiently dense and regular, while for the cotangent Laplacian they will be (almost) tridiagonal and diagonally dominant.

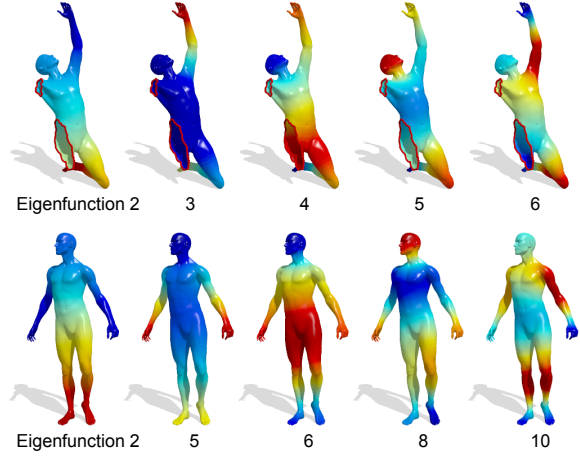


Figure 7: Correspondence between the first ten LB eigenfunctions of two nearly-isometric shapes in presence of partiality. Note the different sequences in the two cases: not all eigenfunctions on the complete shape (in this case, the 3rd, 4th, 7th, and 9th) have a corresponding function on the partial shape. In turn, the last 4 eigenfunctions of the partial shape do not appear among the first 10 of the full shape. In this example, the correspondence between eigenfunctions was obtained by comparing the respective eigenvalues.

Eigenvalue perturbation (rank of \mathbf{C}). Here we take the simplifying assumptions that $\mathbf{L}_{\mathcal{M}}$ and $\mathbf{L}_{\mathcal{N}}$ do not have repeated eigenvalues. Let $\mathbf{L}_{\mathcal{N}} = \Phi^{\top} \mathbf{A} \Phi$ and $\mathbf{L}_{\overline{\mathcal{M}}} = \overline{\Phi}^{\top} \mathbf{A} \overline{\Phi}$ be the spectral decompositions of $\mathbf{L}_{\mathcal{N}}$ and $\mathbf{L}_{\overline{\mathcal{M}}}$ respectively. Following [MH88] we can write the derivative of λ_i eigenvalue of $\mathbf{L}_{\mathcal{N}}$ and, thus, of $\mathbf{L}(0)$, as:

$$\lambda'_i = \phi_i^{\top} \mathbf{D}_{\mathcal{N}} \phi_i = \sum_{v,w \in \partial\mathcal{N}} (\mathbf{D}_{\mathcal{N}})_{vw} \phi_{iv} \phi_{iw} = \langle \phi_i, \phi_i \rangle_{\mathbf{D}_{\mathcal{N}}}. \quad (13)$$

With the expression $\phi_i^{\top} \mathbf{D}_{\mathcal{N}} \phi_i$ we make a slight abuse of notation, as the product should be interpreted over the restriction of ϕ_i to $\partial\mathcal{N}$ or, equivalently, $\mathbf{D}_{\mathcal{N}}$ should be interpreted as being zero-padded to the size of the full mesh.

Note that the first derivative of the eigenvalues only depends on the squared $\mathbf{D}_{\mathcal{N}}$ norm of the corresponding eigenvectors along the boundary. The continuity of the eigenvalues in $\mathbf{L}(t)$ helps in explaining the interleave of the eigenbasis seen in Fig. 7, as the eigenvalues and corresponding eigenvectors of $\mathbf{L}_{\mathcal{N}}$ and $\mathbf{L}_{\overline{\mathcal{N}}}$ overlap with little modifications going towards the full Laplacian $\mathbf{L}(1) = \mathbf{L}_{\mathcal{M}}$. We make use of this fact in order to estimate the rank of \mathbf{C} as the index of the largest eigenvalue of $\mathbf{L}_{\mathcal{N}}$ smaller or equal to the largest eigenvalue of $\mathbf{L}_{\mathcal{M}}$ (see Fig. 6).

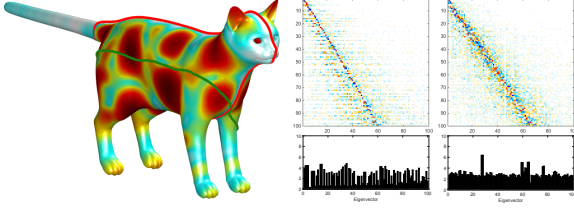


Figure 8: Left: A model is cut in two different ways (red and green curves), each producing a partial shape with different boundary. Function f (16) is plotted over the model. Middle: Ground-truth functional map between the complete model and the partial shape produced by the red cut (top), and values of f along the cut (bottom). Right: Plots associated to the green cut.

Eigenvector perturbation (shape of \mathbf{C}). The eigenvector derivatives for eigenvectors of $\mathbf{L}_{\mathcal{N}}$ are given by

$$\phi'_i = \sum_{\substack{j=1 \\ j \neq i}}^n \frac{\phi_i^\top \mathbf{D}_{\mathcal{N}} \phi_j}{\lambda_i - \lambda_j} \phi_j + \sum_{j=1}^{\bar{n}} \frac{\phi_i^\top \mathbf{E} \bar{\phi}_j}{\lambda_i - \bar{\lambda}_j} \bar{\phi}_j. \quad (14)$$

Note that the second summation has support over $\bar{\mathcal{N}}$ and thus provides the completion of the eigenvector on the missing part. The formula for the second summation is correct only if the eigenvalues of $\mathbf{L}_{\bar{\mathcal{N}}}$ are all distinct from λ_i . If $\mathbf{L}_{\bar{\mathcal{N}}}$ shares some eigenvalues with $\mathbf{L}_{\mathcal{N}}$ the formula would be slightly different [MH88], but it would still only have support over $\bar{\mathcal{N}}$, hence providing eigenvector completion.

On the other hand, the first summation is responsible for the modifications of the eigenvectors over the nodes \mathcal{N} . Here the numerator has a term $\phi_i^\top \mathbf{D}_{\mathcal{N}} \phi_j$ which, since $\mathbf{D}_{\mathcal{N}}$ is band-diagonal and diagonally dominant, acts as a dot product of the eigenvectors over the boundary layer, thus pointing to large mixing of eigenvectors with a strong co-presence near the boundary. In turn, the term $\lambda_i - \lambda_j$ at the denominator forces a strong mixing of eigenvectors corresponding to similar eigenvalues. This results in an amplification of the variation for higher eigenvalues, as eigenvalues tend to densify on the higher end of the spectrum. This results in a spread of the functional map for higher frequencies, as can be seen from the examples in Fig. 4 and 8.

Remark. The first-order modification in the eigenvectors within \mathcal{N} , which determines the shape of \mathbf{C} , is due only to eigenvector interactions along the boundary. It is not a function of the missing area, as intuition may suggest.

As a consequence, the variation of the eigenvectors due to the mixing within the partial shape can be reduced either by shortening the boundary, or by reducing the strength of the boundary interaction. This can be done by selecting a boundary along which eigenvectors with similar eigenvalues are either orthogonal, or both small.

We can measure the variation of the eigenbasis as a function of the boundary \mathcal{B} splitting \mathcal{M} into \mathcal{N} and $\bar{\mathcal{N}}$ as

$$\partial \Phi(\mathcal{B}) = \sum_{i=1}^n \|\phi'_i\|_{\mathcal{N}}^2 = \sum_{i=1}^n \left(\sum_{\substack{j=1 \\ j \neq i}}^n \frac{\phi_i^\top \mathbf{D}_{\mathcal{N}} \phi_j}{\lambda_i - \lambda_j} \right)^2. \quad (15)$$

In Fig. 8 we see an example of two different cuts with different interaction strengths. The function plotted on the cat model is

$$f(v) = \sum_{\substack{i,j=1 \\ i \neq j}}^n \left(\frac{\phi_{iv} \phi_{jv}}{\lambda_i - \lambda_j} \right)^2. \quad (16)$$

Assuming $\mathbf{D}_{\mathcal{N}}$ diagonal and with constant diagonal elements k , then we have

$$k \int_{\mathcal{B}} f(v) dv \geq \partial \Phi(\mathcal{B}), \quad (17)$$

in fact:

$$\begin{aligned} \partial \Phi(\mathcal{B}) &\approx k \sum_{i=1}^n \left(\sum_{\substack{j=1 \\ j \neq i}}^n \frac{\sum_{v \in \partial \mathcal{M}} \phi_{iv} \phi_{jv}}{\lambda_i - \lambda_j} \right)^2 \\ &\leq k \sum_{v \in \partial \mathcal{M}} \sum_{\substack{i,j=1 \\ i \neq j}}^n \left(\frac{\phi_{iv} \phi_{jv}}{\lambda_i - \lambda_j} \right)^2 = k \sum_{v \in \partial \mathcal{M}} f(v). \end{aligned} \quad (18)$$

The cuts plotted in Fig. 8 have same length, but one cut goes along a symmetry axis of the shape and through low values of f , while the other goes through rather high values of f . As a result we see that in the first case a lot of the eigenvectors are preserved and the functional map is tight along the slanted diagonal, while in the second case all the eigenvectors vary by a large amount and the corresponding functional map is more dispersed.

6. Experimental results

Datasets. In the literature there has been a general lack of benchmarks aimed at evaluating the performance of matching methods under partiality transformations. Here we introduce two datasets to tackle this more challenging scenario. As base models, we use shapes from the TOSCA dataset [BBK08], consisting of 76 nearly-isometric shapes subdivided into 8 classes. Each class comes with a “null” shape in a standard pose, and ground-truth correspondences are provided for all shapes within the same class. In order to make the datasets more challenging and avoid compatible triangulations, all shapes were remeshed in advance to 10k vertices by iterative pair contractions [GH97]. We processed the shapes in two different ways:

Regular cuts. The null shape of each class is cut with a plane using 6 different orientations, including an exact cut along the symmetry plane (note that each null shape has

an extrinsic bilateral symmetry). The 6 cuts are then transferred to the remaining poses using the ground-truth correspondence, resulting in 456 partial shapes in total. Some examples are shown in Fig. 2, 6, and 7.

Irregular holes. Given a shape and an “area budget” telling the amount of surface area to keep, we derive additional shapes by an erosion process applied to the surface. Specifically, seed holes are placed at a few farthest samples over the shape; the holes are then enlarged until the specified area budget is attained. We do so for all shapes in TOSCA and for area budgets equal to 40%, 70%, and 90% of the total surface area, resulting in a total amount of 684 shapes. Examples of this dataset are shown in Fig. 10, 13.

Where not specified otherwise, we use 120 random partial shapes for the first dataset and 80 for the second, equally distributed among the different classes. Each partial shape is then matched to the null shape of the corresponding class.

Error measure. As quantitative measure for correspondence quality we use the error criterion originally introduced in [KLF11] to evaluate the quality of point-wise maps. The input quantity is a functional map \mathbf{C} , which is converted to a point-wise counterpart by using the nearest-neighbor approach described in [OBCS*12]. We plot cumulative curves showing the percent of matches which have error smaller than a variable threshold. Finally, we write p_e to denote the (normalized) area below these curves up to error level e .

6.1. Data term

Due to the particular nature of the problem, in all our experiments we only make use of dense, *local* descriptors as

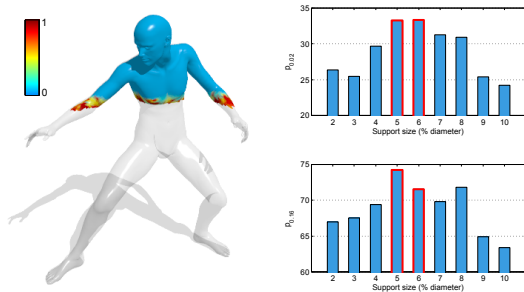


Figure 9: Left: Normalized L_2 distance between local point descriptors on a partial shape (body top) and the corresponding descriptors on the complete shape (in transparent white). Points close to the boundary have larger distance due to missing parts. Right: Bar plots showing the local and global accuracy of our matching method, as we increase the support of local descriptors. Small neighborhoods induce sensitivity to surface noise, whereas descriptors with large support are affected by boundary effects. The optimal values are found in-between (red frames).

	SHOT	SHOT+MS	SHOT+IH	All
cat ($p_{0.16}$)	79.21	78.87	76.54	77.67
victoria ($p_{0.16}$)	79.64	80.02	76.90	77.82
cat ($p_{0.02}$)	33.85	33.99	32.58	32.94
victoria ($p_{0.02}$)	32.55	32.50	31.50	31.95

Table 1: Performance comparison on a representative subset of TOSCA (regular cuts) under different local descriptors as the data term. We show results in terms of both global ($p_{0.16}$) and local ($p_{0.02}$) accuracy.

a data term. This is in contrast with the more common scenario in which full shapes are being matched – thus allowing to employ more robust, globally-aware features such as landmark matches, repeatable surface regions, and various spectral quantities [OBCS*12].

Local descriptors. We experimented with several choices of descriptors, driven both by efficiency and accuracy considerations. In particular, we used combinations of SHOT [TSDS10], Mesh Saliency (MS) [LVJ05], and Integral Hashes (IH) [ART15]. Other robust descriptors such as curvature and Integral Invariants [PWHY09] were also tested, but ultimately excluded from the analysis due to their sensitivity to surface noise or large amounts of partiality (resulting, for instance, in inconsistent voxelizations in the case of [PWHY09]). We remark that all the considered descriptors are based on *extrinsic* quantities. SHOT was computed using 10 normal bins (352 dimensions), while both IH and MS were evaluated over 5 scales (5 dimensions each).

In Table 1 we report a performance comparison of our method on the TOSCA dataset (regular cuts), with different descriptor combinations as the data term.

Support size. Since the descriptors are defined on a local neighborhood at each point, it is natural to ask to what extent the size of the support plays a role in the matching accuracy. For this purpose, we analyzed the performance of our method across increasing support sizes. The results of this experiment, together with an illustration of the boundary effects due to partiality, are given in Fig. 9. We emphasize that, differently from other methods [ART15, PBB13] which ignore points close to the boundary in order to avoid boundary effects, in our formulation we retain *all* shape points. This is motivated by our choice of a robust norm for the data term, as also depicted in Fig. 2.

6.2. Sensitivity analysis

We conducted a set of experiments aimed at evaluating the sensitivity of our approach to different parametrizations. As in the previous section, in order to reduce overfitting we only used a subset of TOSCA (regular cuts), namely composed of the *cat* and *victoria* shape classes (20 pairs).

Rank. In the first experiment we study the change in accuracy as the rank of the functional map is increased; this

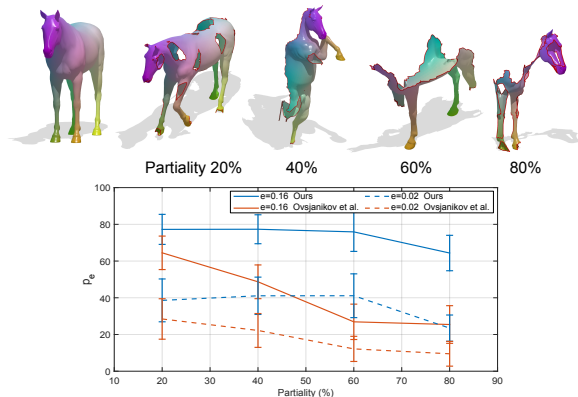


Figure 10: Comparisons with the baseline functional maps pipeline in terms of $p_{0.02}$ and $p_{0.16}$ at increasing levels of partiality. The two methods perform comparably well at low partiality; as the amount of missing parts increases, our method maintains high accuracy (example solutions on top) while the quality of [OBCS*12] drops significantly.

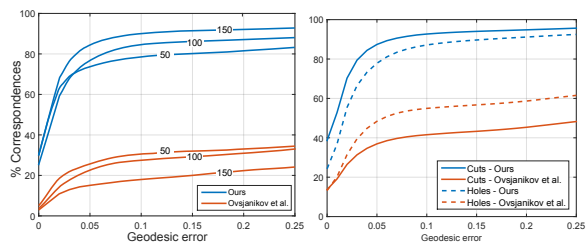


Figure 11: Left: Correspondence quality obtained on a subset of TOSCA at increasing rank (reported as labels on top of the curves). Right: Full comparisons on the TOSCA datasets “regular cuts” and “irregular holes”.

corresponds to using an increasing number of basis functions for the two shapes being matched. For this experiment we compare with the baseline method of Ovsjanikov *et al.* [OBCS*12] by using the same dense descriptors as ours. For fair comparisons, we did not impose map orthogonality or operator commutativity constraints [OBCS*12], which cannot obviously be satisfied due to partiality. The results of this experiment are reported in Fig. 11 (left). As we can see from the plots, our method allows to obtain more accurate solutions as the rank increases, while an opposite behavior is observed for the other method.

Representation. Our method is general enough to be applied to different shape representations, as long as a proper discretization of the Laplace operator is available. In Fig. 12 we show some qualitative examples of correspondences produced by our algorithm on point clouds, where we used the method described in [BSW09] to construct a discrete Laplacian. Due to the non-rigid deformations the point cloud is



Figure 12: Partial functional correspondence with point clouds. Similar colors encode corresponding points.

allowed to undergo, this is traditionally considered a particularly challenging problem, with few methods currently capable of giving satisfactory solutions without exploiting controlled conditions or domain-specific information (*e.g.*, the knowledge that the shape being matched is that of a human). These are, to the best of our knowledge, the best results to be published so far for this particular class of problems.

6.3. Comparisons

We compared our method with the baseline approach of Ovsjanikov *et al.* [OBCS*12] on both datasets (200 shape pairs in total); the results are shown in Fig. 11 (right). As an additional experiment, we compared the two methods across increasing amounts of partiality. The rationale behind this experiment is to show that, at little or no partiality, our approach converges to the one described in [OBCS*12], currently among the state of the art in non-rigid shape matching. However, as partiality increases so does the sensitivity of the latter method. Fig. 10 shows the results of this experiment.

Parameters for our method were chosen on the basis of the previous analysis. Specifically, we used dense SHOT descriptors as data, $k = 100$ eigenfunctions per shape, and set $\mu_1 = \mu_3 = 1$, $\mu_4 = \mu_5 = 10^3$, and $\mu_2 = 10^2$. Additional examples of partial matchings obtained with our method are shown in Fig. 13 and in the supplementary material.

7. Discussion and conclusions

In this paper we tackled the problem of dense matching of deformable shapes under partiality transformations. We cast our formulation within the framework of functional maps, which we adapted and extended to deal with this more challenging scenario. Our approach is fully automatic and makes

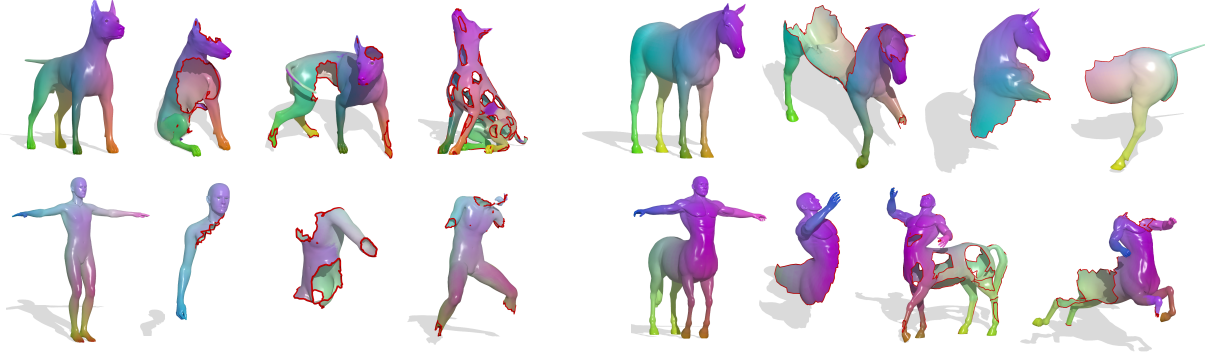


Figure 13: Examples of partial functional correspondence obtained with our method on the proposed datasets. Notice how regions close to the boundary are still accurately matched despite the noisy descriptors.

exclusive use of dense local features as a measure of similarity. Coupled with a robust prior on the functional correspondence derived from a perturbation analysis of the shape Laplacians, this allowed us to devise an effective optimization process with remarkable results on very challenging cases. In addition to our framework for partial functional correspondence we also introduced two new datasets comprising hundreds of shapes, which we hope will foster further research on this challenging problem.

One of the main issues of our method concerns the existence of multiple optima, which is in turn related to the presence of non-trivial self-isometries on the considered manifolds. Since most natural shapes are endowed with intrinsic symmetries, one may leverage this knowledge in order to avoid inconsistent matchings. For example, including a smoothness prior on the correspondence might alleviate such imperfections and thus provide better-behaved solutions. Secondly, since the main focus of this paper is on tackling partiality rather than general deformations, our current formulation does not explicitly address the cases of topological changes and inter-class similarity (e.g., matching a man to a gorilla). However, the method can be easily extended to employ more robust descriptors such as pairwise features [RABT13, VKZH13], or to simultaneously optimize over ad-hoc functional bases on top of the correspondence. Finally, extending our approach to tackle entire shape collections, as opposed to individual pairs of shapes, represents a further exciting direction of research.

Appendix A - Discretization

We describe more in depth the discretization steps and give the implementation details of our algorithm (we skip trivial derivations for the sake of compactness). Detailed gradients for each term are given in Appendix B.

Mesh parametrization. We denote by S a triangle mesh of n points, composed of triangles S_j for $j = 1, \dots, m$. In the

following derivations, we will consider the classical triangle-based parametrization described by the charts $x_j : \mathbb{R}^2 \rightarrow \mathbb{R}^3$

$$x_j(\alpha, \beta) = x_{j,1} + \alpha(x_{j,2} - x_{j,1}) + \beta(x_{j,3} - x_{j,1}), \quad (19)$$

with $\alpha \in [0, 1]$ and $\beta \in [0, 1 - \alpha]$. With $x_{j,k} \in \mathbb{R}^3$ we denote the 3D coordinates of vertex $k \in \{1, 2, 3\}$ in triangle S_j .

Each triangle S_j is equipped with a discrete metric tensor with coefficients

$$g_j = \begin{pmatrix} E_j & F_j \\ F_j & G_j \end{pmatrix}, \quad (20)$$

where $E_j = \|x_{j,2} - x_{j,1}\|^2$, $F_j = \langle x_{j,2} - x_{j,1}, x_{j,3} - x_{j,1} \rangle$, and $G_j = \|x_{j,3} - x_{j,1}\|^2$. The volume element for the j -th triangle is then given by $\sqrt{\det g_j} = \sqrt{E_j G_j - F_j^2}$.

Integral of a scalar function. Scalar functions $f : S \rightarrow \mathbb{R}$ are assumed to behave linearly within each triangle. Hence, $f(x(\alpha, \beta))$ is a linear function of (α, β) and it is uniquely determined by its values at the vertices of the triangle. The integral of f over S_j is then simply given by:

$$\begin{aligned} & \int_0^1 \int_0^{1-\alpha} f(\alpha, \beta) \sqrt{\det g_j} d\beta d\alpha & (21) \\ &= \iint f(0,0)(1-\alpha-\beta) + f(1,0)\alpha + f(0,1)\beta \sqrt{\det g_j} d\beta d\alpha \\ &= \frac{1}{6} (f(0,0) + f(1,0) + f(0,1)) \sqrt{E_j G_j - F_j^2} \\ &= \frac{1}{3} (f(0,0) + f(1,0) + f(0,1)) \text{area}(S_j), & (22) \end{aligned}$$

where $f(0,0) = f(x_{j,1})$, $f(1,0) = f(x_{j,2})$, and $f(0,1) = f(x_{j,3})$.

Gradient of a scalar function. For the intrinsic gradient of f we get the classical expression in local coordinates:

$$\nabla f = \begin{pmatrix} \frac{\partial x_j}{\partial \alpha} & \frac{\partial x_j}{\partial \beta} \end{pmatrix} \begin{pmatrix} E_j & F_j \\ F_j & G_j \end{pmatrix}^{-1} \begin{pmatrix} f_\alpha \\ f_\beta \end{pmatrix}, \quad (23)$$

where we write f_α to denote the partial derivative $\frac{\partial f}{\partial \alpha} = f_{j,2} - f_{j,1}$ and similarly for f_β . The norm of the intrinsic gradient over triangle S_j is then given by:

$$\begin{aligned} \|\nabla f\| & \quad (24) \\ &= \sqrt{\langle \nabla f, \nabla f \rangle} \\ &= \sqrt{\begin{pmatrix} f_\alpha & f_\beta \end{pmatrix} \begin{pmatrix} E_j & F_j \\ F_j & G_j \end{pmatrix}^{-1} \begin{pmatrix} f_\alpha \\ f_\beta \end{pmatrix}} \\ &= \sqrt{\begin{pmatrix} f_\alpha & f_\beta \end{pmatrix} \begin{pmatrix} G_j & -F_j \\ -F_j & E_j \end{pmatrix} \begin{pmatrix} f_\alpha \\ f_\beta \end{pmatrix} \frac{1}{\det g_j}} \\ &= \sqrt{\frac{f_\alpha^2 G_j - 2f_\alpha f_\beta F_j + f_\beta^2 E_j}{\det g_j}}. \end{aligned} \quad (25)$$

Note that, since we take f to be linear, the gradient ∇f is constant within each triangle. We can then integrate ∇f over S_j as follows:

$$\begin{aligned} \int_{S_j} \|\nabla f(x)\| \sqrt{\det g_j} d\alpha d\beta & \quad (26) \\ &= \int_{S_j} \sqrt{\frac{f_\alpha^2 G_j - 2f_\alpha f_\beta F_j + f_\beta^2 E_j}{\det g_j}} \sqrt{\det g_j} d\alpha d\beta \\ &= \int_{S_j} \sqrt{f_\alpha^2 G_j - 2f_\alpha f_\beta F_j + f_\beta^2 E_j} d\alpha d\beta \\ &= \frac{1}{2} \sqrt{f_\alpha^2 G_j - 2f_\alpha f_\beta F_j + f_\beta^2 E_j}. \end{aligned} \quad (27)$$

In the following, we write \mathcal{N} and \mathcal{M} to denote the partial and full shape respectively. Further, let $\{\lambda_i^{\mathcal{N}}\}_{i=1,\dots,k}$ be the first k eigenvalues of the Laplacian on \mathcal{N} , and similarly for $\{\lambda_i^{\mathcal{M}}\}_{i=1,\dots,k}$. The functional map \mathbf{C} has size $k \times k$.

Mumford-Shah functional (μ_2 -term). Following Equations (22) and (27), we immediately obtain:

$$\begin{aligned} \int_S \xi(v) \|\nabla v\| dx & \\ &= \sum_{j=1}^m \int_{S_j} \xi(\alpha, \beta) \|\nabla v\| \sqrt{\det g_j} d\beta d\alpha \\ &= \sum_{j=1}^m \sqrt{v_\alpha^2 G_j - 2v_\alpha v_\beta F_j + v_\beta^2 E_j} \int_{S_j} \xi(\alpha, \beta) d\beta d\alpha \\ &\approx \frac{1}{6} \sum_{j=1}^m \sqrt{v_\alpha^2 G_j - 2v_\alpha v_\beta F_j + v_\beta^2 E_j} (\xi(0,0) + \xi(1,0) + \xi(0,1)), \end{aligned}$$

where $\xi(0,0) = \xi(v(x_{j,1}))$, $\xi(1,0) = \xi(v(x_{j,2}))$, and $\xi(0,1) = \xi(v(x_{j,3}))$.

Weight matrix (μ_3 -term). Recall from Section 5 and Figure 6 that an estimate for the rank of \mathbf{C} can be easily computed as

$$r = \max\{i \mid \lambda_i^{\mathcal{N}} < \max_j \lambda_j^{\mathcal{M}}\}. \quad (28)$$

We use this information in order to construct the weight matrix \mathbf{W} , whose diagonal slope directly depends on r .

To this end, we model \mathbf{W} as a regular $k \times k$ grid in \mathbb{R}^2 . The slanted diagonal of \mathbf{W} is a line segment $\mathbf{d}(t) = \mathbf{p} + t \frac{\mathbf{n}}{\|\mathbf{n}\|}$ with $t \in \mathbb{R}$, where $\mathbf{p} = (1,1)^\top$ is the matrix origin, and $\mathbf{n} = (1, r/k)^\top$ is the line direction with slope r/k . The high-frequency spread in \mathbf{C} is further accounted for by funnel-shaping \mathbf{W} along the slanted diagonal. We arrive at the following expression for \mathbf{W} :

$$w_{ij} = e^{-\sigma \sqrt{i^2 + j^2}} \frac{\mathbf{n}}{\|\mathbf{n}\|} \times ((i,j)^\top - \mathbf{p})\|, \quad (29)$$

where the second factor is the distance from the slanted diagonal \mathbf{d} , and $\sigma \in \mathbb{R}_+$ regulates the spread around \mathbf{d} . In our experiments we set $\sigma = 0.03$.

Orthogonality (μ_4, μ_5 -terms). For practical reasons, we incorporate the off-diagonal and diagonal terms within one term with the single coefficient $\mu_{4,5}$. In addition, we rewrite the off-diagonal penalty using the following equivalent expression:

$$\sum_{i \neq j} (\mathbf{C}^\top \mathbf{C})_{ij}^2 = \|\mathbf{C}^\top \mathbf{C}\|_{\mathbb{F}}^2 - \sum_i (\mathbf{C}^\top \mathbf{C})_{ii}^2. \quad (30)$$

Vector $\mathbf{d} \in \mathbb{R}^k$ is constructed by setting the first r elements (according to (28)) equal to 1, and the remaining $k - r$ elements equal to 0.

Appendix B - Gradients

We find local solutions to each optimization problem by the (nonlinear) conjugate gradient method. In this Section we give the detailed gradient derivations of all terms involved in the optimization.

In order to keep the derivations practical, we will model function v by its corresponding n -dimensional vector \mathbf{v} . Note that, depending on the optimization step, the gradients are computed with respect to either \mathbf{v} or \mathbf{C} .

Data term (w.r.t. v). Let q denote the number of corresponding functions between the two shapes. Matrices \mathbf{F} and \mathbf{G} contain the column-stacked functions defined over \mathcal{N} and \mathcal{M} and have size $n \times q$. The respective projections onto the corresponding functional spaces Φ and Ψ are stored in the $k \times q$ matrices \mathbf{A} and \mathbf{B} respectively. Let us write \mathbf{H}_{ij} to identify the elements of the matrix $\mathbf{CA} - \mathbf{B}(\eta(v))$, we then have

$$\begin{aligned} & \frac{\partial}{\partial v_p} \|\mathbf{CA} - \mathbf{B}(\eta(v))\|_{2,1} \\ &= \frac{\partial}{\partial v_p} \sum_{j=1}^q \left(\sum_{i=1}^n \mathbf{H}_{ij}^2 \right)^{\frac{1}{2}} \\ &= \sum_{j=1}^q \left(\sum_{i=1}^n \mathbf{H}_{ij}^2 \right)^{-\frac{1}{2}} \sum_{i=1}^n \mathbf{H}_{ij} \frac{\partial}{\partial v_p} \mathbf{H}_{ij}. \end{aligned} \quad (31)$$

Since $\mathbf{B}(\eta(v))_{ij} = \sum_k^n \Psi_{ik}^T \eta(v_k) \mathbf{F}_{kj}$, we have:

$$\frac{\partial}{\partial v_p} \mathbf{H}_{ij} = \frac{\partial}{\partial v_p} [\mathbf{C} \mathbf{A}_{ij} - \mathbf{B}_{ij}] = \Psi_{ip}^T \mathbf{F}_{pj} \frac{\partial}{\partial v_p} \eta(v_p). \quad (32)$$

Finally:

$$\frac{\partial}{\partial v_p} \eta(v_p) = 1 - \tanh^2(2v_p - 1). \quad (33)$$

Area term (μ_1 -term w.r.t. v). The derivative of the discretized area term is:

$$\begin{aligned} & \frac{\partial}{\partial v_p} \frac{1}{9} \left(\sum_{i=1}^n (S_{\mathcal{N}})_i - \sum_{i=1}^n (S_{\mathcal{M}})_i \eta(v_i) \right)^2 \\ &= \frac{2}{9} \left(\sum_{i=1}^n (S_{\mathcal{N}})_i - \sum_{i=1}^n (S_{\mathcal{M}})_i \eta(v_i) \right) S_M \frac{\partial}{\partial v_p} \eta(v_p) \end{aligned}$$

where $(S_{\mathcal{M}})_i$ and $(S_{\mathcal{N}})_i$ are the local area elements associated with the i -th vertex of meshes \mathcal{M} and \mathcal{N} respectively. For the derivative of $\eta(v_p)$ see equation (33).

Mumford-Shah functional (μ_2 -term w.r.t. v). Computing the gradient $\nabla_{\mathbf{v}} \int_S \xi(\mathbf{v}) \|\nabla \mathbf{v}\| dx$ involves computing partial derivatives of $\xi(\mathbf{v})$ with respect to \mathbf{v} . These are simply given by:

$$\begin{aligned} \frac{\partial}{\partial v_k} \xi(v_k) &= \frac{\partial}{\partial v_k} e^{-\frac{\tanh(2v_k-1)}{4\sigma^2}} \\ &= -\frac{1 - \tanh^2(2v_k-1)}{2\sigma^2} e^{-\frac{\tanh(2v_k-1)}{4\sigma^2}}. \end{aligned}$$

In the following derivations we set $D_j \equiv \sqrt{v_\alpha^2 G_j - 2v_\alpha v_\beta F_j + v_\beta^2 E_j}$, and $D_j = 0$ whenever $\nabla \mathbf{v} = \mathbf{0}$. The gradient of the Mumford-Shah functional is then composed of the partial derivatives:

$$\begin{aligned} & \frac{\partial}{\partial v_k} \int_S \xi(\mathbf{v}) \|\nabla \mathbf{v}\| dx \\ &= \sum_{j=1}^m \frac{\partial}{\partial v_k} \int_{S_j} \xi(\mathbf{v}) \|\nabla \mathbf{v}\| \\ &= \frac{1}{6} \sum_{j \in N(k)} \frac{\partial}{\partial v_k} D_j (\xi(v_k) + \xi(v_{j,2}) + \xi(v_{j,3})) \\ &= \frac{1}{6} \sum_{j \in N(k)} (\xi(v_k) + \xi(v_{j,2}) + \xi(v_{j,3})) \frac{\partial}{\partial v_k} D_j + D_j \frac{\partial}{\partial v_k} \xi(v_k) \\ &= \frac{1}{6} \sum_{j \in N(k)} (\xi(v_k) + \xi(v_{j,2}) + \xi(v_{j,3})) \frac{1}{2} \frac{1}{D_j} \frac{\partial}{\partial v_k} D_j^2 + D_j \frac{\partial}{\partial v_k} \xi(v_k) \\ &= \frac{1}{6} \sum_{j \in N(k)} (\xi(v_k) + \xi(v_{j,2}) + \xi(v_{j,3})) K_j + D_j \frac{\partial}{\partial v_k} \xi(v_k) \end{aligned}$$

where we write $K_j \equiv \frac{1}{D_j} ((v_k - v_{j,2})(G_j - F_j) + (v_k - v_{j,3})(E_j - F_j))$, and $j \in N(k)$ are the indices of the triangles containing the k -th vertex. Note that we slightly abuse notation by writing $v_k, v_{j,2}$, and $v_{j,3}$ to denote the three vertices of the j -th triangle, even though in general the ordering might be different depending on the triangle.

Data term (w.r.t. \mathbf{C}). The derivative of the data term with respect to \mathbf{C} is similar to (31). The only difference is in the partial derivative:

$$\frac{\partial}{\partial \mathbf{C}_{pq}} \mathbf{H}_{ij} = \frac{\partial}{\partial \mathbf{C}_{pq}} \sum_{i=1}^k \mathbf{C}_{ik} \mathbf{A}_{kj} = \begin{cases} \mathbf{C}_{pq} \mathbf{A}_{qj} & \text{if } i = p \\ 0 & \text{otherwise.} \end{cases} \quad (34)$$

Weight matrix (μ_3 -term w.r.t. \mathbf{C}). This is simply given by:

$$\frac{\partial}{\partial \mathbf{C}_{pq}} \|\mathbf{C} \circ \mathbf{W}\|_{\mathbb{F}}^2 = \mathbf{C}_{pq} (\mathbf{W}_{pq})^2. \quad (35)$$

Orthogonality ($\mu_{4,5}$ -term w.r.t. \mathbf{C}). The gradient of the last term can be finally obtained as:

$$\begin{aligned} & \frac{\partial}{\partial \mathbf{C}_{pq}} \left[\|\mathbf{C}^T \mathbf{C}\|_{\mathbb{F}}^2 - \sum_i (\mathbf{C}^T \mathbf{C})_{ii}^2 + \sum_i ((\mathbf{C}^T \mathbf{C})_{ii} - d_i)^2 \right] \\ &= 4(\mathbf{C} \mathbf{C}^T \mathbf{C})_{pq} + 2 \sum_i \left[-\sum_k \mathbf{C}_{ki}^2 \frac{\partial}{\partial \mathbf{C}_{pq}} \sum_k \mathbf{C}_{ki}^2 + (\sum_k \mathbf{C}_{ki}^2 - d_i) \frac{\partial}{\partial \mathbf{C}_{pq}} \sum_k \mathbf{C}_{ki}^2 \right] \\ &= 4[(\mathbf{C} \mathbf{C}^T \mathbf{C})_{pq} - d_q \mathbf{C}_{pq}]. \end{aligned}$$

References

- [AMCO08] AIGER D., MITRA N. J., COHEN-OR D.: 4-points congruent sets for robust pairwise surface registration. *TOG* 27, 3 (2008), 85. 1
- [ART15] ALBARELLI A., RODOLÀ E., TORSELLO A.: Fast and accurate surface alignment through an isometry-enforcing game. *Pattern Recognition* 48 (2015), 2209–2226. 1, 8
- [BB08] BRONSTEIN A. M., BRONSTEIN M. M.: Not only size matters: regularized partial matching of nonrigid shapes. In *Proc. NORDIA* (2008). 1, 3, 5
- [BBBK09] BRONSTEIN A., BRONSTEIN M., BRUCKSTEIN A., KIMMEL R.: Partial similarity of objects, or how to compare a centaur to a horse. *IJCV* 84, 2 (2009), 163–183. 1
- [BBK06] BRONSTEIN A. M., BRONSTEIN M. M., KIMMEL R.: Generalized multidimensional scaling: a framework for isometry-invariant partial surface matching. *PNAS* 103, 5 (2006), 1168–1172. 1
- [BBK08] BRONSTEIN A., BRONSTEIN M., KIMMEL R.: *Numerical Geometry of Non-Rigid Shapes*. Springer, 2008. 7
- [BMAS14] BOUMAL N., MISHRA B., ABSIL P.-A., SEPULCHRE R.: Manopt, a Matlab toolbox for optimization on manifolds. *Journal of Machine Learning Research* 15 (2014), 1455–1459. URL: <http://www.manopt.org>. 5
- [BSW09] BELKIN M., SUN J., WANG Y.: Constructing laplace operator from point clouds in rd. In *Proc. SODA* (2009), Society for Industrial and Applied Mathematics, pp. 1031–1040. 9
- [BWW*14] BRUNTON A., WAND M., WUHRER S., SEIDEL H.-P., WEINKAUF T.: A low-dimensional representation for robust partial isometric correspondences computation. *Graphical Models* 76, 2 (2014), 70–85. 1
- [Duf59] DUFFIN R. J.: Distributed and lumped networks. *Journal of Mathematics and Mechanics* 8, 5 (1959), 793–826. 4
- [GH97] GARLAND M., HECKBERT P. S.: Surface simplification using quadric error metrics. In *Proc. SIGGRAPH* (1997), pp. 209–216. 7

- [HG13] HUANG Q.-X., GUIBAS L.: Consistent shape maps via semidefinite programming. *Computer Graphics Forum* 32, 5 (2013), 177–186. 2
- [HWG14] HUANG Q., WANG F., GUIBAS L. J.: Functional map networks for analyzing and exploring large shape collections. *TOG* 33, 4 (2014), 36. 2
- [KLCF10] KIM V. G., LIPMAN Y., CHEN X., FUNKHOUSER T. A.: Möbius transformations for global intrinsic symmetry analysis. *Comput. Graph. Forum* 29, 5 (2010), 1689–1700. 1
- [KLF11] KIM V. G., LIPMAN Y., FUNKHOUSER T. A.: Blended intrinsic maps. *TOG* 30, 4 (2011), 79. 1, 8
- [LVJ05] LEE C. H., VARSHNEY A., JACOBS D. W.: Mesh saliency. *ACM Trans. Graph.* 24, 3 (2005), 659–666. 8
- [Mac49] MACNEAL R. H.: *The solution of partial differential equations by means of electrical networks*. PhD thesis, California Institute of Technology, 1949. 4
- [MDSB03] MEYER M., DESBRUN M., SCHRÖDER P., BARR A. H.: Discrete differential-geometry operators for triangulated 2-manifolds. *Visualization&Mathematics* (2003), 35–57. 4, 5
- [MH88] MURTHY D. V., HAFTKA R. T.: Derivatives of eigenvalues and eigenvectors of a general complex matrix. *Intl. J. Numer. Met. Eng.* 26, 2 (1988), 293–311. 5, 6, 7
- [MS89] MUMFORD D., SHAH J.: Optimal approximations by piecewise smooth functions and associated variational problems. *Comm. Pure and Applied Math.* 42, 5 (1989), 577–685. 3
- [OBCS*12] OVSJANIKOV M., BEN-CHEN M., SOLOMON J., BUTSCHER A., GUIBAS L.: Functional maps: a flexible representation of maps between shapes. *ACM Trans. Graph.* 31, 4 (July 2012), 30:1–30:11. 2, 3, 4, 5, 8, 9
- [PBB13] POKRASS J., BRONSTEIN A. M., BRONSTEIN M. M.: Partial shape matching without point-wise correspondence. *Numer. Math. Theor. Meth. Appl.* 6 (2013), 223–244. 2, 8
- [PP93] PINKALL U., POLTHIER K.: Computing discrete minimal surfaces and their conjugates. *Experimental mathematics* 2, 1 (1993), 15–36. 4
- [PWHY09] POTTMANN H., WALLNER J., HUANG Q.-X., YANG Y.-L.: Integral invariants for robust geometry processing. *Comput. Aided Geom. Des.* 26, 1 (2009), 37–60. 8
- [RABT13] RODOLÀ E., ALBARELLI A., BERGAMASCO F., TORSELLO A.: A scale independent selection process for 3d object recognition in cluttered scenes. *International Journal of Computer Vision* 102, 1-3 (2013), 129–145. 10
- [RBA*12] RODOLÀ E., BRONSTEIN A., ALBARELLI A., BERGAMASCO F., TORSELLO A.: A game-theoretic approach to deformable shape matching. In *Proc. CVPR* (June 2012), pp. 182–189. 2
- [SY14] SAHILLIOĞLU Y., YEMEZ Y.: Partial 3-d correspondence from shape extremities. *Computer Graphics Forum* 33, 6 (2014), 63–76. 2
- [TSDS10] TOMBARI F., SALTI S., DI STEFANO L.: Unique signatures of histograms for local surface description. In *Proc. ECCV* (2010), pp. 356–369. 8
- [VC02] VESE L. A., CHAN T. F.: A multiphase level set framework for image segmentation using the Mumford and Shah model. *IJCV* 50, 3 (2002), 271–293. 3
- [VKTS*11] VAN KAICK O., TAGLIASACCHI A., SIDI O., ZHANG H., COHEN-OR D., WOLF L., HAMARNEH G.: Prior knowledge for part correspondence. *Computer Graphics Forum* 30, 2 (2011), 553–562. 2
- [vKZH13] VAN KAICK O., ZHANG H., HAMARNEH G.: Bilateral maps for partial matching. *Computer Graphics Forum* 32, 6 (2013), 189–200. 2, 10
- [VKZHCO11] VAN KAICK O., ZHANG H., HAMARNEH G., COHEN-OR D.: A survey on shape correspondence. *Computer Graphics Forum* 30, 6 (2011), 1681–1707. 1
- [ZSCO*08] ZHANG H., SHEFFER A., COHEN-OR D., ZHOU Q., VAN KAICK O., TAGLIASACCHI A.: Deformation-driven shape correspondence. *Computer Graphics Forum* 27, 5 (2008), 1431–1439. 1